

Optimal displacement detection of arbitrarily-shaped levitated dielectric objects using optical radiation

Shaun Laing,¹ Shelby Klomp,² George Winstone,² Alexey Grinin,² Andrew Dana,²
Zhiyuan Wang,² Kevin Seca Widyatmodjo,² James Bateman,¹ and Andrew A. Geraci³

¹*Physics Department, Faculty of Science and Engineering, Swansea University, Swansea SA2 8PP, UK*

²*Center for Fundamental Physics, Department of Physics and Astronomy,
Northwestern University, Evanston, Illinois 60208, USA*

³*Center for Fundamental Physics and Center for Interdisciplinary Exploration and Research in Astrophysics,
Department of Physics and Astronomy, Northwestern University, Evanston, Illinois 60208, USA*

(Dated: September 4, 2024)

Optically-levitated dielectric objects are promising for precision force, acceleration, torque, and rotation sensing due to their extreme environmental decoupling. While many levitated optomechanics experiments employ spherical objects, for some applications non-spherical geometries offer advantages. For example, rod-shaped or dumbbell shaped particles have been demonstrated for torque and rotation sensing and high aspect ratio plate-like particles can exhibit reduced photon recoil heating and may be useful for high-frequency gravitational wave detection or as high bandwidth accelerometers. To achieve optimal sensitivity, cooling, and quantum control in these systems, it is beneficial to achieve optimal displacement detection using scattered light. We describe and numerically implement a method based on Fisher information that is applicable to suspended particles of arbitrary geometry. We demonstrate the agreement between our method and prior methods employed for spherical particles, both in the Rayleigh and Lorentz-Mie regimes. As practical examples we analyse the optical detection limits of an optically-levitated high-aspect-ratio disc-like dielectric object and a rod-shaped object for configurations recently realized in experimental work.

I. INTRODUCTION

Optimal position and momentum measurements are important for many applications of optical tweezers. In life- and material sciences, efficient detection allows for lower laser powers and thus less perturbation of the object under study [1, 2]. For precision measurements in quantum-optomechanical systems, detection efficiency also impacts displacement sensitivity due to shot noise and radiation pressure back-action [3] and determines the lowest temperature achievable for the center-of-mass motion of the suspended particle when applying feedback cooling. Levitated optomechanics, where an object for example is suspended with radiation pressure, diamagnetic levitation, or radio-frequency electromagnetic fields, is a platform that features excellent decoupling from the environment, leading to a number of applications in precision sensing, quantum science, materials science, and non-equilibrium physics. For recent reviews see Refs. [4–6]. The information that can be attained regarding the displacement of a levitated particle via scattering of optical radiation has been quantified in recent literature using the information radiation pattern (IRP) [7–9]. The information radiation pattern will generally depend on the observation direction, the shape of the particle, and the detection method.

The theory of optimal position detection for the Rayleigh regime has been studied in [7] and for Mie-spheres in [8, 9]. While dipolar scatterers and Mie-spheres are frequently encountered cases, particles of other shapes, particularly high-aspect-ratio disks and rods, dumbbells, and hollow spheres, are optimal for many applications. For instance, rod-shaped or dumb-

bell shaped particles are well-suited for sensitive torque and rotation sensing [10–13] and high aspect ratio plate-like particles can exhibit reduced photon recoil heating for high bandwidth accelerometers or the detection of high-frequency gravitational waves with frequencies exceeding a few kHz [14, 15]. It is therefore of interest to develop a method to provide a practical means to calculate IRPs for experimental configurations which include scatterers of arbitrary shape. Furthermore it is of practical interest to consider how realistic detection schemes can approach the ideal theoretical limits for the IRP for useful levitated particle geometries.

In this paper we present a method for determining the optimal interferometric position measurement for arbitrarily-shaped dielectric objects and derive equations for their radiation information patterns. The method we present is based on the Fisher information and agrees with the methods shown in Refs. [7] and [8, 9] for spherical particles, while generalizing it to arbitrary shapes. We demonstrate several numerical implementations using the SCUFF-EM package [16, 17], the pyGDM package [18, 19], and the COMSOL Multiphysics [20] package to determine the IRPs for disks, rods, and spheres. In addition to the center of mass degrees of freedom corresponding to translational motion, we analyze and discuss rotational and torsional degrees of freedom of non-spherically symmetric objects and possible coupling between the different degrees of freedom.

This paper is structured as follows. In Sec. II we describe the theoretical approach being used for determining the radiation information pattern based on Fisher information. In Sec. III we describe its numerical implementation in several computational packages and con-

duct a comparison of the results. In Sec. IV we present and discuss numerical IRPs in a focused Gaussian beam trap and counter propagating beam trap for an ideal reference field for spheres, plates, and rods. For the case of Mie scattering by spheres, we show the equivalence between our results and those in Ref. [8]. In section V, we present an example of numerical results for lab-relevant Gaussian reference fields and propose detector geometries for practical imaging configurations. Finally we conclude with a discussion of future applications of relevance to the optomechanics community, including the detection of high frequency gravitational waves.

II. THEORETICAL APPROACH

In Ref. [8] the information radiation pattern for light scattered by Mie spheres was calculated by considering the quantum theory of excitation of exact eigenmodes of the electromagnetic field in the presence of the dielectric sphere at equilibrium. To compute the information radiation pattern for a scatterer of generalized geometry, we adopt the method of computing the Fisher information in the scattered radiation field [21, 22]. A similar approach was recently used to determine the information radiation pattern for reflective geometries [23]. The Fisher information carried by an electromagnetic wave scattered in the far field into a differential solid angle $d\Omega$ in the direction (θ, ϕ) can be expressed as

$$\bar{S}^{\text{FI}}(\theta, \phi)_\mu = \frac{2}{\hbar\omega} \text{Re} \left(\frac{\partial}{\partial \mu} \vec{E}^*(\theta, \phi) \times \frac{\partial}{\partial \mu} \vec{H}(\theta, \phi) \right), \quad (1)$$

where \vec{E} and \vec{H} are the electric and magnetic fields of the scattered radiation, respectively, and $\mu \in (x, y, z, \theta_x, \theta_y, \theta_z)$ is the coordinate along which the motion of the trapped particle is being described by the information field.

III. NUMERICAL METHODS APPLIED TO CALCULATE EM FIELDS FOR A SPHERE FROM MULTIPLE NUMERICAL MODELS

In this section we describe the numerical implementation of the Fisher information method using three different computational back-ends. We include a comparison of the relative advantages and limitations of each computational package.

SCUFF-EM (Surface Current/Field Formulation of ElectroMagnetism) is an open-source implementation of the surface integral equation/boundary-element method (SIE/BEM) to solve electromagnetic scattering problems [17, 24]. Starting with a known geometry in some medium (this could be a vacuum, a fluid, or a gas) and illuminating the geometry with some known incident EM field, we can use these techniques to find the unknown scattered field. As a numerical solver, the scatterer must

be discretized. We mesh the object we are interested in using a set of roughly equal triangles. Each interior edge of the mesh is given a basis function $\vec{f}_n(\vec{r})$ which represents the surface currents [25]. These basis functions are used to solve the following linear system,

$$\langle \vec{f}_m | \mathbf{\Gamma}^{EE} | \vec{f}_n \rangle \vec{k} = -\langle \vec{f}_m | \vec{E}^{\text{inc}} \rangle \quad (2)$$

where $\mathbf{\Gamma}^{AB}$ is the 3×3 Dyadic Green's function giving the field of type A from the surface current of type B , \vec{E}^{inc} is the incident electric field, and \vec{k} is a vector of the surface current expansion vectors k_n . The scattered electric and magnetic fields at a point \vec{r} are given by,

$$\vec{E}_s(\vec{r}) = \sum_n k_n \int \mathbf{\Gamma}^{EE}(\vec{r}, \vec{r}') \vec{f}_n(\vec{r}') d\vec{r}' \quad (3)$$

$$\vec{H}_s(\vec{r}) = \sum_n k_n \int \mathbf{\Gamma}^{ME}(\vec{r}, \vec{r}') \vec{f}_n(\vec{r}') d\vec{r}' \quad (4)$$

respectively [16].

Another numerical method we use is pyGDM[19, 26], which is the Python toolkit for full-field electro-dynamical simulations of nano-structures based on the Green Dyadic Method (GDM). Similar to the couple dipole approximation, pyGDM calculates the optical response of an arbitrary shaped object by discretizing volume of the object into a sum over finite size volume elements the in Lippmann-Schwinger equation

$$\vec{E}(\vec{r}_i) = \vec{E}^{\text{inc}}(\vec{r}_i) + \sum_{j=1}^N \mathbf{S}_0^{EE}(\vec{r}_i, \vec{r}_j) \cdot \chi_e(\vec{r}_j) \cdot \vec{E}(\vec{r}_j) V_{\text{cell}} \quad (5)$$

where \vec{E}^{inc} is the incident electric field, \mathbf{S}_0^{EE} is the field-susceptibility tensor, which is closely related to the Dyadic Green's function $\mathbf{\Gamma}^{EE}$ [27]; χ_e is the susceptibility of the structure, and \vec{r}_i is the position of each volume element V_{cell} . Then one can construct a $3N$ -dimensional vector to represent the ensemble of all the electric field of the finite volume element for the incident field or the scattered field $\vec{E}_{obj}^{\text{inc}}$ or \vec{E}_{obj} and use a generalized field propagator \mathbf{K} , which is a $3N \times 3N$ matrix describing the response of the entire structure. Once the generalized propagator \mathbf{K} is known, we can calculate the response of the system to arbitrary monochromatic incident fields by a matrix-vector,

$$\vec{E}_{obj} = \mathbf{K} \cdot \vec{E}_{obj}^{\text{inc}}. \quad (6)$$

In addition to SCUFF-EM and pyGDM, we also use COMSOL Multiphysics which is a simulation software that uses the finite element method to solve partial differential equations relevant to many physics problems. In this case, the *Wave Optics Module* is used to simulate scattered electric fields within the *Electromagnetic Waves, Frequency Domain* Interface. Similarly

Package	Mesh Topology	Scaling	Method
SCUFF-EM	Area	A^4	Boundary element
PyGDM2	Volume	V^3	Green's Dyadic
COMSOL	Volume	Adaptive	Variable

TABLE I. Comparison of numerical methods used to generate scattered electric fields.

to our other methods, the known geometry and incident EM fields must be defined, but in COMSOL a perfectly matched layer is implemented to create the correct boundary conditions at the edges of the simulation, and the volume of the scatterer and the surrounding volume is discretized. The mesh is determined by the physics of the problem within COMSOL to be primarily tetrahedral with a minimum of 5 mesh elements per wavelength. The solver computes the near field scattered fields in the entire geometry by iteratively computing Maxwell's equations for all mesh points. The calculation relies on a biconjugate gradient stabilized iterative method [20]. Then the far field electric field is calculated from the near field on a particular surface S enclosing the particle, by using the Stratton-Chu formula,

$$\vec{E}_{\text{far}}(\theta, \phi) = \frac{ik}{4\pi} \vec{r}_0 \times \int [\vec{n} \times \vec{E} - \eta \vec{r}_0 \times (\vec{n} \times \vec{H})] e^{ik\vec{r} \cdot \vec{r}_0} dS \quad (7)$$

where \vec{r}_0 is the unit vector in the direction of radius vector \vec{r} which points from the origin to the surface S , \vec{n} is the unit normal to the surface S , and η is the impedance $\eta = \sqrt{\mu/\epsilon}$.

The three methods that we used for the numerical calculation of the scattered fields are listed in Table I, where we compare the factors that contribute to the efficiency of the method. The meshing in PyGDM and COMSOL is done for the volume of the entire relevant geometry, which can be computationally taxing for large geometries. In PyGDM, the mesh elements are equally sized throughout the geometry, so the scaling of computation time goes as the cube of the volume (i.e. the cube of the number of elements). COMSOL has the advantage of adaptive meshing, where the physics of the problem is taken into consideration in the generation of the mesh. For example, the mesh is often finest on the particle surface, but has the minimum spacing of 5 mesh elements per wavelength farther away. Additionally, in the calculation of IRPs, it is important that the surface that is used to generate the far field in Eq. 7 has a sufficiently fine mesh. SCUFF-EM, on the other hand, uses methods where the calculation is done only on the surface of the particle, so the mesh is an evenly spaced triangular mesh, and the computation time scales with the surface area of the scatterer. For this reason, SCUFF-EM often has much shorter computation times for large particle geometries.

Another important factor in the comparison of these methods is the solver type. Unlike PyGDM and SCUFF-EM which use fixed methods and solvers with different

memory and CPU overheads[16, 18], COMSOL uses a selection of direct and iterative solvers that it will choose from based on the physics of the problem being solved. For the scattering problems discussed here, COMSOL primarily employed the biconjugate gradient stabilized (BiCGStab) iterative method.

In order to convert the numerically calculated scattered fields into information radiation patterns we must measure how the field changes on some measurement sphere in the far field regime as the particle moves in one axis. We achieve this by measuring the scattered field some distance r from the origin with the particle located at $-l$ and $+l$ where the distance $2l \ll \lambda$ such that the change in the field as we move from $-l$ to $+l$ is linear. We find the complex scattered electric and magnetic fields $\vec{E}^{\pm l}(\theta, \phi)$ and $\vec{H}^{\pm l}(\theta, \phi)$ at each point (θ, ϕ) on the measurement sphere when the particle is located at either $-l$ or $+l$. This measurement sphere is made up of hypothetical detectors each covering a solid angle $d\Omega$. To find the Fisher information flux Eq. (1) we find each component of the change of each field as the first-order central-difference approximation to the derivative,

$$\frac{\partial E_j^*}{\partial \mu} = \frac{E_j^{*+} - E_j^{*-}}{l - (-l)} \quad (8)$$

$$\frac{\partial H_j}{\partial \mu} = \frac{H_j^+ - H_j^-}{l - (-l)} \quad (9)$$

where $j \in (x, y, z)$ is the component of the field in cartesian coordinates, and μ is the axis the object is moved through. By inserting Eqs. (8) and (9) into Eq. (1), we find the Fisher information flux and thus the information patterns are found as,

$$\mathcal{I}_\mu(\theta, \phi) = \vec{S}^{\text{FI}}(\theta, \phi) \cdot \vec{A}_i \quad (10)$$

where \vec{A}_i is the area vector of the i th detector located at (θ, ϕ) and points out of the sphere.

There also exist some approximate analytic solutions for the scattered electric field for dielectric particles which could be used to compute IRP's and can be used to benchmark the numerical methods. An example of this is in [28] which utilizes the Rayleigh-Gans approximation and the Rayleigh approximation for small particles. This method effectively treats each point of the dielectric as a Rayleigh scatterer, and considers the electric field on the interior of the dielectric to be constant. For a dielectric with smallest dimension d_{min} and largest dimension d_{max} illuminated by light of wavelength λ , these approximations hold when $d_{\text{min}} \ll d_{\text{max}}$ and $d_{\text{min}} \ll \lambda$. This method has been shown to produce electromagnetic scattering patterns for high aspect ratio dielectric discs which match numerical simulations.

IV. RESULTS FOR SPHERES, PLATES, RODS

Using the Fisher information approach, we can calculate information radiation patterns for novel experimen-

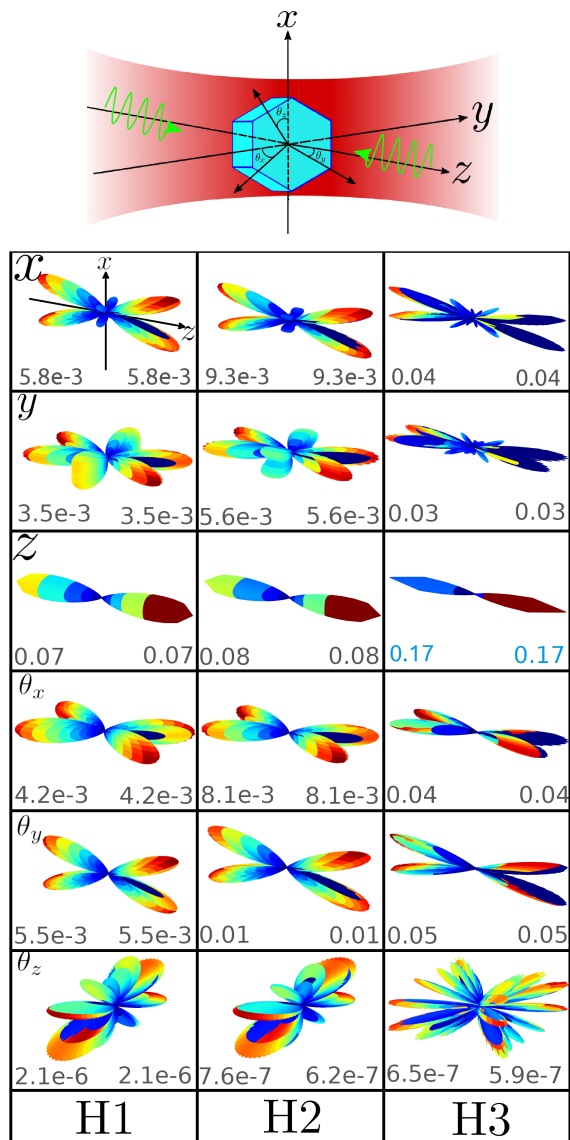


FIG. 1. (upper) A hexagonal plate levitated in a standing wave optical trap and labelled coordinates corresponding to the displayed information radiation patterns. Laser fields are linearly polarized along the x - direction and propagating along the z - direction. Angles $\theta_x, \theta_y, \theta_z$ represent rotations about the x -, y - and z - axes, respectively. (lower) IRPs from the SCUFF-EM implementation for each degree of freedom μ of a hexagonal disk trapped in a standing wave trap made up of two counter-propagating beams with a beam waist of $w_0 = 12\mu\text{m}$. Each plate has dimensions given in Table II. We also show the detection efficiencies for the left and right focusing lenses each with a numerical aperture of $\text{NA} = 0.041$.

tally relevant geometries including hexagonal plates and cylindrical rods. Results for a hexagonal plate trapped in a standing wave similar to the experimental configuration described in Ref. [15] are shown in Fig. 1. We consider three sizes of plates labelled H1, H2, and H3 with dimensions given in Table II. The IRPs generated

Batch Name	Thickness	Diameter
H1	300 nm	$2.5 \mu\text{m}$
H2	200 nm	$3 \mu\text{m}$
H3	200 nm	$5 \mu\text{m}$

TABLE II. Dimensions of the hexagonal plates considered in the text. These dimensions roughly correspond to those reported in recent experimental work in Ref. [15]

by these plates are given in Fig. 1 for a beam waist of $w_0 = 12\mu\text{m}$. We also show the detection efficiencies for a lens to the left and a lens to the right. These are given in the lower corners of each panel. The detection efficiencies are calculated as,

$$\eta_\mu = \int_{S_d} \mathcal{I}_\mu(\theta, \phi) \sin \theta d\theta d\phi \quad (11)$$

where S_d is the solid angle covered by the collection lens. Blue detection efficiencies indicate a value greater than $1/9$, which is necessary for ground state cooling via active feedback cooling, as discussed in Ref. [7].

We generally see that the information radiation pattern has a structure containing lobes. Assuming the laser propagates along \hat{z} , for the x and y motions, the main lobes are oriented in the $x-z$ and $y-z$ planes, respectively. For motion in the z axis the information is almost entirely concentrated in the $\pm z$ directions. These results are unsurprising as the scattered radiation from lasers incident on the face of the flat plate tends to be emitted primarily in the forwards and backwards directions. The information radiation patterns obtained for the rotational degrees of freedom are also unsurprising. The θ_x and θ_y motion both produce lobes in the directions consistent with the direction light will primarily scatter into under rotations about those axes. Lobes corresponding to θ_x and θ_y rotations are visible in $y-z$ and $x-z$ planes, respectively. The θ_z motion primarily produces lobes radial to the laser propagation direction. These result from the change in the angle of the radial faces on the hexagon and the detection efficiency for this motion is rather poor compared with rotations about the other two axes, as expected. We also note that, in general, the detection efficiencies increase with the hexagon diameter. This corresponds with more of the IRP being concentrated forwards and backward as the diameter increases. However, in the θ_z rotation, this is not the case. As the detection efficiency for this motion is generally quite small, being only associated with the hexagonal edge corners, we attribute the observed variations also to poor numerical precision associated with the discrete grid of positions at which we measure the IRP.

Nanorods are another novel geometry that has gained much interest recently [29]. Trapping a rod in a standing wave, as shown in Fig. 2 will generate IRPs as shown in Fig. 2. We consider two sizes of rods that are described in Table III. The IRPs for the librational degrees of freedom in the smaller R1 rod match the results for

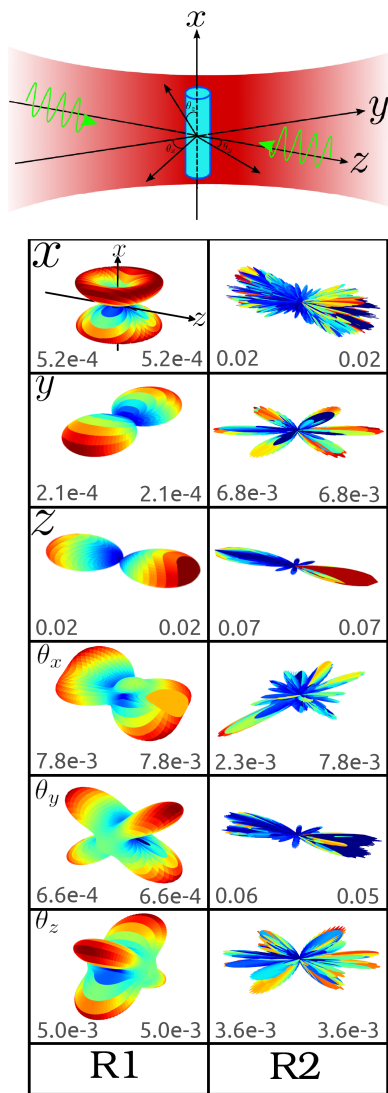


FIG. 2. (upper) A rod levitated in a standing wave optical trap. Angles $\theta_x, \theta_y, \theta_z$ represent rotations about the x -, y - and z - axes, respectively. (lower) IRPs from the SCUFF-EM implementation for each degree of freedom μ of a rod trapped in a standing wave trap made up of two counter-propagating beams with a beam waist of $w_0 = 12\mu\text{m}$. The rods have the dimensions given in Table III. We also show the detection efficiencies for the left and right focusing lenses each with a numerical aperture of $\text{NA} = 0.041$.

the point-like dipole. This is to be expected as the dimensions are sufficiently sub-wavelength. We also note a predicted information pattern for the θ_x rotation. This is initially surprising as a cylindrical rod would display symmetry in this direction. We believe this to be due to a numerical artifact associated with the discrete geometry triangulation that does not display this exact symmetry.

Finally, in order to validate our numerical method, we reproduce the results for spheres trapped in a single-beam trap as given in [8]. Fig. 3 we compare the theoretical results obtained with the method of Ref. [8] with

Rod Name	Diameter	Length
R1	$0.108\mu\text{m}$	$0.795\mu\text{m}$
R2	$1.55\mu\text{m}$	$9.024\mu\text{m}$

TABLE III. Dimensions of the rods considered in the text and in Fig. 2. The R1 rods are based on the nanorods used in Ref. [30] while the R2 rods dimensions are arbitrarily chosen to have a diameter equal to the laser wavelength, and a length close to the beam waist to ensure we are no longer in the point-like regime.

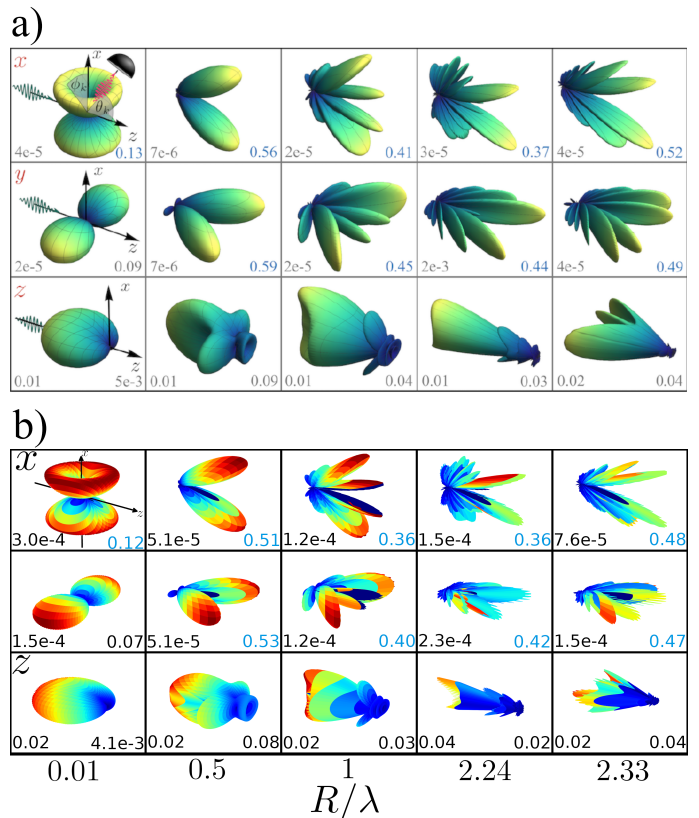


FIG. 3. Information patterns for varying radii of spherical particles in a Gaussian beam traveling in the positive z direction. The beam is focused by a lens to the left with a numerical aperture of $\text{NA} = 0.1$. a) Shows the analytical results reproduced from [8] and b) are the numerical results from SCUFF-EM. The numbers in the bottom corners of each panel refer to the detection efficiencies η_μ for a lens to the left and to the right. The left collection lens is the same as the focusing lens, while the right collection lens has a numerical aperture of $\text{NA} = 0.75$.

numerical results as obtained from SCUFF-EM. Reasonable agreement is obtained between the two methods, with small differences attributed to discretization of the spherical geometry in a finite mesh and numerical precision of the relevant derivatives needed to evaluate Eq. 1.

V. COMPARISON WITH INTERFEROMETRY USING A PRACTICAL REFERENCE FIELD

In the previous section, we have determined the information radiation patterns achievable for levitated objects of varying shape according to the theoretical limit from the Fisher information, subject to constraints from quantum radiation pressure back-action and shot noise. To generate an interferometric detection of the particles motion in the laboratory, for example using homodyne detection, one must interfere the scattered light from the particle with another laser beam which is taken as a reference. In this section we compare the detection efficiency achievable with an example of a reference beam corresponding to a recent experiment [15]. In particular, a simple reference field to implement is to use one of the trapping beams. In our simulations, we find the IRP with a reference field by taking the scattered field from our chosen back end and imposing the field from a single trapping beam in our analysis code. We then simply observe how the electric field changes at the position (θ, ϕ) as we change the degree of freedom we are interested in. A comparison of the theoretical Fisher information radiation with the information scattered using a reference beam for the H3 hexagon is shown in Fig. 4. Here the collection lens corresponds to an effective numerical aperture of approximately 0.043, and under these conditions the trap laser reference beam is less than 25 percent as efficient as the theoretical limit. Nevertheless this approach can be used to benchmark the sensitivity of practical interferometry setups relative to the best achievable.

VI. CONCLUSION

In this paper we have described a general method to numerically determine the information radiation patterns for dielectric particles of arbitrary shape based on a computation of the Fisher information. We have demonstrated the equivalence of the numerical results we obtain when using the Fisher information method and the analytic results for spherical Mie scattering described in Ref. [8, 9]. We have applied our method to commonly used non-spherical geometries in levitated optomechanics, including hexagonal high aspect ratio prisms and nanorods. Our method is broadly applicable to the optomechanics community for a wide range of trappable species commonly used in levitated optomechanics experiments. Our approach also permits the calculation of the detection efficiency for interferometric detection with realistic reference laser beam configurations, which can be useful for experimental groups to determine the best imaging setups to achieve center of mass and rotational cooling of trapped dielectric objects of non-spherical geometry. For example, such an approach can be beneficial for levitated optomechanical sensors which realize their ideal sensitivity by having a non-spherical shape, including rods or

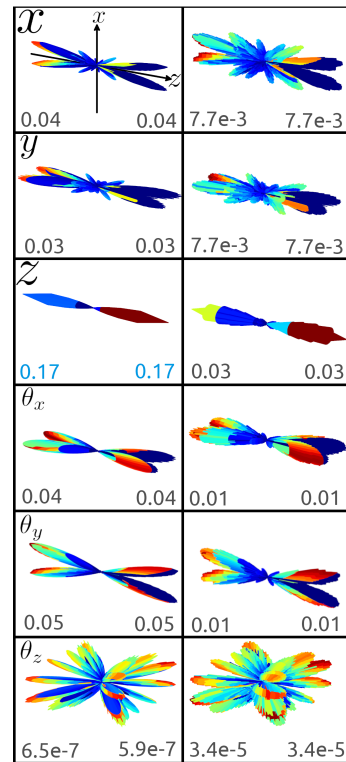


FIG. 4. The information pattern for a H3 hexagonal plate in a counter-propagating beam trap with a beam waist of $w_0 = 12\mu\text{m}$. The left set of panels are the IRPs created using the Fisher information approach discussed in the main text. The panels on the right use one of the trapping beams as a reference field. These IRPs are generated by interfering the scattered electric field with the electric field from a single Gaussian beam and taking the differential of this total field with respect to the change in the degree of freedom considered.

dumbbells for rotation sensing or high aspect ratio plate like particles for the application of high frequency gravitational wave detection above the frequency range of 10 kHz [14, 15].

VII. APPENDIX

In this appendix we include the results from the code SCUFF-EM for information radiation patterns for varying radii of spherical particles for different trapping and imaging numerical apertures to facilitate an additional comparison with the results in Ref. [8]. We consider a Gaussian beam traveling in the positive z direction. For the results shown in Fig. 5, the beam is focused by a lens to the left with a numerical aperture of $\text{NA} = 0.75$ which is also used as the left collection lens for the detection efficiencies. The right collection lens also has a numerical aperture of $\text{NA} = 0.75$. In addition to the comparison shown directly in Fig. 3, our results can be compared with those for similar numerical apertures as shown in

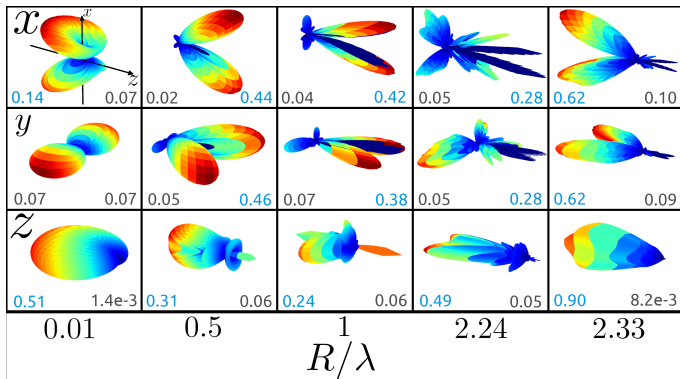


FIG. 5. Information patterns from SCUFF-EM for varying radii of spherical particles in a Gaussian beam traveling in the positive z direction. The beam is focused by a lens to the left with a numerical aperture of $NA = 0.75$ which is also used as the left collection lens for the detection efficiencies. The right collection lens also has a numerical aperture of $NA = 0.75$.

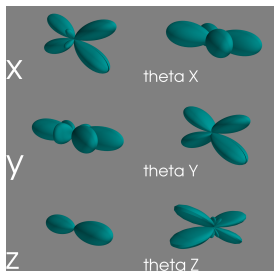


FIG. 6. Shape of Information radiation pattern calculated for the H1 hexagon for the same beam parameters as chosen in Fig. 1 for the SCUFF-EM computational package.

Ref. [8], and show reasonable quantitative agreement.

Here we also provide a comparison between the results obtained using the packages SCUFF-EM and pyGDM2 for the H1 hexagon, to verify the general shape of the information radiation pattern when computed using different numerical back-ends. The results displayed in Fig. 6 can be compared with the first column of plots displayed in Fig. 1. Apart from the θ_z term, for which the radiation carries little information regarding the orientation for rotations about the axis of the prism, there is reasonable qualitative agreement for all other degrees of freedom shown. The θ_z motion is not easily discerned in the proposed setup with the beam parameters chosen as can be evidenced by the many orders of magnitude smaller values of the efficiency as compared to the other angular motions and translational degrees of freedom.

ACKNOWLEDGEMENTS

We are grateful to Oriol Romero-Isart for helpful discussions which contributed significantly to the development of this work. We thank Patrick Maurer for assistance with comparison of our results with Lorentz-Mie scattering by dielectric spheres. AAG is supported in part by NSF grants PHY-2110524 and PHY-2111544, the Heising-Simons Foundation, the John Templeton Foundation, and ONR Grant N00014-18-1-2370. AAG and GW are supported by the W.M. Keck Foundation. AG is supported by the Alexander von Humboldt foundation. SL is also supported by EPSRC International Quantum Technologies Network Grant EP/W02683X/1 and is grateful for EPSRC support through Standard Research Studentship (DTP) EP/R51312X/1. This work used the Quest computing facility at Northwestern.

-
- [1] C. J. Bustamante, Y. R. Chemla, S. Liu, and M. D. Wang, Optical tweezers in single-molecule biophysics, *Nature Reviews Methods Primers* **1**, 25 (2021).
 - [2] K. C. Neuman, E. H. Chadd, G. F. Liou, K. Bergman, and S. M. Block, Characterization of photodamage to escherichia coli in optical traps, *Biophysical Journal* **77**, 2856 (1999).
 - [3] M. Aspelmeyer, T. J. Kippenberg, and F. Marquardt, Cavity optomechanics, *Rev. Mod. Phys.* **86**, 1391 (2014).
 - [4] J. Millen, T. S. Monteiro, R. Pettit, and A. N. Vamivakas, Optomechanics with levitated particles, *Reports on Progress in Physics* **83**, 026401 (2020).
 - [5] C. Gonzalez-Ballester, M. Aspelmeyer, L. Novotny, R. Quidant, and O. Romero-Isart, Levitodynamics: Levitation and control of microscopic objects in vacuum, *Science* **374**, eabg3027 (2021), <https://www.science.org/doi/pdf/10.1126/science.abg3027>.
 - [6] D. C. Moore and A. A. Geraci, Searching for new physics using optically levitated sensors, *Quantum Science and Technology* **6**, 014008 (2021).
 - [7] F. Tebbenjohanns, M. Frimner, and L. Novotny, Optimal position detection of a dipolar scatterer in a focused field, *Physical Review A* **100**, 043821 (2019).
 - [8] P. Maurer, C. Gonzalez-Ballester, and O. Romero-Isart, Quantum theory of light interaction with a lorentz-mie particle: Optical detection and three-dimensional ground-state cooling, *Phys. Rev. A* **108**, 033714 (2023).
 - [9] P. Maurer, C. Gonzalez-Ballester, and O. Romero-Isart, Erratum: Quantum theory of light interaction with a lorentz-mie particle: Optical detection and three-dimensional ground-state cooling [phys. rev. a 108, 033714 (2023)], *Phys. Rev. A* **109**, 019901 (2024).
 - [10] J. Ahn, Z. Xu, J. Bang, Y.-H. Deng, T. M. Hoang, Q. Han, R.-M. Ma, and T. Li, Optically levitated nanodumbbell torsion balance and ghz nanomechanical rotor, *Phys. Rev. Lett.* **121**, 033603 (2018).
 - [11] R. Reimann, M. Doderer, E. Hebestreit, R. Diehl, M. Frimner, D. Windey, F. Tebbenjohanns, and L. Novotny, Ghz rotation of an optically trapped nanoparticle in vacuum, *Phys. Rev. Lett.* **121**, 033602 (2018).

- [12] F. Monteiro, S. Ghosh, E. C. van Assendelft, and D. C. Moore, Optical rotation of levitated spheres in high vacuum, *Phys. Rev. A* **97**, 051802 (2018).
- [13] Z. Xu and T. Li, Detecting casimir torque with an optically levitated nanorod, *Phys. Rev. A* **96**, 033843 (2017).
- [14] N. Aggarwal, G. P. Winstone, M. Teo, M. Baryakhtar, S. L. Larson, V. Kalogera, and A. A. Geraci, Searching for new physics with a levitated-sensor-based gravitational-wave detector, *Physical Review Letters* **128**, 111101 (2022).
- [15] G. Winstone, Z. Wang, S. Klomp, G. R. Felsted, A. Laeuger, C. Gupta, D. Grass, N. Aggarwal, J. Sprague, P. J. Pauzaskie, *et al.*, Optical trapping of high-aspect-ratio nayf hexagonal prisms for khz-mhz gravitational wave detectors, *Physical review letters* **129**, 053604 (2022).
- [16] H. Reid, Surface Integral Equations and Boundary Element Method, <https://homerreid.github.io/SCUFFEM-TutorialSymposium/BEMTalk.20120318.pdf> (2012).
- [17] M. T. Reid, Scuff-EM, <http://github.com/homerreid/scuff-EM> (2018).
- [18] P. R. Wiecha, pygdm-a python toolkit for full-field electro-dynamical simulations and evolutionary optimization of nanostructures, *Computer Physics Communications* **233**, 167 (2018).
- [19] P. R. Wiecha, C. Majorel, A. Arbouet, A. Patoux, Y. Brûlé, G. C. Des Francs, and C. Girard, “pygdm”-new functionalities and major improvements to the python toolkit for nano-optics full-field simulations, *Computer Physics Communications* **270**, 108142 (2022).
- [20] www.comsol.com, Comsol multiphysics (2024).
- [21] O. Romero-Isart, private communication (2023).
- [22] J. Hüpfel, F. Russo, L. M. Rachbauer, D. Bouchet, J. Lu, U. Kuhl, and S. Rotter, Continuity equation for the flow of fisher information in wave scattering, *Nature Physics* 10.1038/s41567-024-02519-8 (2024).
- [23] R. Gajewski and J. Bateman, Backaction suppression in levitated optomechanics using reflective boundaries (2024), arXiv:2405.04366 [physics.optics].
- [24] M. T. H. Reid and S. G. Johnson, Efficient computation of power, force, and torque in bem scattering calculations, *IEEE Transactions on Antennas and Propagation* **63**, 3588 (2015).
- [25] D. R. Wilton, S. S. Rao, and A. W. Glisson, Electromagnetic Scattering By Surfaces of Arbitrary Shape., National Bureau of Standards, Special Publication (1980).
- [26] C. Girard, Near fields in nanostructures, *Reports on Progress in Physics* **68**, 1883 (2005).
- [27] G. S. Agarwal, Quantum electrodynamics in the presence of dielectrics and conductors. i. electromagnetic-field response functions and black-body fluctuations in finite geometries, *Phys. Rev. A* **11**, 230 (1975).
- [28] R. Schiffer and K. O. Thielheim, Light scattering by dielectric needles and disks, *J. Appl. Phys.* **1** **50**, 10.1063/1.326257 (1979).
- [29] S. Kuhn, A. Kosloff, B. A. Stickler, F. Patolsky, K. Hornberger, M. Arndt, and J. Millen, Full rotational control of levitated silicon nanorods, *Optica* **4**, 356 (2017).
- [30] S. Kuhn, P. Asenbaum, A. Kosloff, M. Sclafani, B. A. Stickler, S. Nimmrichter, K. Hornberger, O. Cheshnovsky, F. Patolsky, and M. Arndt, Cavity-Assisted Manipulation of Freely Rotating Silicon Nanorods in High Vacuum, *Nano Letters* **15**, 5604 (2015), arXiv:1506.04881.